Local Conduction at the $BiFeO_3$-$CoFe_2O_4$ Tubular Oxide Interface

*Ying-Hui Hsieh, Jia-Ming Liou, Bo-Chao Huang, Chen-Wei Liang, Qing He, Qian Zhan, Ya-Ping Chiu, Yi-Chun Chen, and Ying-Hao Chu**

Interfaces have emerged as focal points of current condensed matter physics. In strongly correlated oxides, heterointerfaces provide a powerful route to create and manipulate the charge, spin, orbital, and lattice degrees of freedom[1] and suggest new possibilities for next generation devices.[2] The most explored interface is artificially constructed heterointerfaces (**Figure 1**(a)). The interaction of degrees of freedom at the interface has resulted in a number of exciting discoveries including the observation of a 2-D electron gas-like behavior at $LaAlO_3$-$SrTiO_3$ (STO) interfaces;[3,4] the emergence of the ferromagnetism in a superconducting material at $YBa_2Cu_3O_{7-x}$-$La_{0.7}Ca_{0.3}MnO_3$ interface[5] and a induced ferromagnetic state in heterointerface between $BiFeO_3$ (BFO) and $La_{0.7}Sr_{0.3}MnO_3$ layer.[6] In ferroic oxides, domain walls dictate a natural homo-interfaces (Figure 1(b)) as a consequence of the minimization of electrostatic and elastic energies. Recently, several key studies have pointed out interesting observations on domain walls in multiferroics, including an insulating interlocked ferroelectric and structural antiphase domain walls in $YMnO_3$ system,[7] the source of the exchange bias interaction between the ferromagnetic metal layer and multiferroic,[8,9] and local conduction at domain walls in BFO[10] and $Pb(Zr,Ti)O_3$.[11] These complex oxide interfaces create a huge playground to discover new emergent phenomena. The key question we would like to address in this manuscript is: is there any other type of complex oxide interfaces? Will we be able to create intriguing functionalities by designing new type of complex oxide interfaces? In order to search for new types of complex oxide interfaces, we must go back to examine the existing oxide heterostructures. Building upon numerous widely demonstrated oxide interfaces, there is one category interesting us: epitaxial self-assembling nano-composites.[12] Such nanostructures have been shown to enhance or create properties by interface-mediated coupling or local confinement, such as magnetoelectricity,[13] ferroelectrcitiy,[14] and low field driven large magneto-resistance.[15] However, systematical study has not been deciphered on the interfacial properties in these nano-composites. The tubular oxide interfaces (Figure 1(c)), surrounding $BiFeO_3$(BFO)-$CoFe_2O_4$(CFO) vertical interface, a key concept in nano-composites interfaces, has been demonstrated in nanowire society in a lot of core-shell structures,[16,17] which is a hint to re-invent the interface between strongly correlated systems. In this letter, we show the local conduction located at the vertical interfaces of BFO-CFO heterostructure evidenced by conduction atomic force microscopy and cross-sectional scanning tunneling microscopy. Such results open new pathways to create and design intriguing interfacial properties of complex oxide tubular interfaces.

100 nm BFO-CFO composite films on 30 nm $SrRuO_3$ (SRO) buffered STO (001) were prepared by pulsed laser deposition assisted with high-pressure reflective high-energy electron difraction to in situ monitor the growth process.[18] In order to study this interface, we employed the conductive atomic force microscope (CAFM), an effective technique to probe local conduction at oxide homo-interfaces with nanoscale spatial resolution such as domain walls in ferroics.[10,11] The spatial resolution of this technique is limited by the tip radius (~20 nm). In **Figure 2**(a), we show the typical morphology of BFO-CFO nanostructure on SRO/STO(001). Due to the surface energy anisotropy, the spinel component forms nanopillars embedded in the perovskite matrix.[19] It is understood that the spinel crystal prefers to form an octahedron with eight (111) surfaces, because of the lowest surface energy at these planes.[20] Revealed by atomic force microscopy, the pyramid-like surface topography of the BFO-CFO heterostructures is observed. The lattice parameters of BFO and CFO, calculated according to the XRD angles (not shown), are 4.02 Å and 8.36 Å, respectively. It suggests that BFO matrix is subjected to epitaxial strains attributed from the substrate-film lattice mismatch, but CFO is fully relaxed. Detailed XRD suggests that the epitaxial relation is $CFO(001)_c[100]_c \| STO(001)_c[100]_c$.[18] Epitaxy in this kind of the system makes it a model system to explore the conceptual tubular oxide interfaces.

Figure 2(b) shows the examination of the conducting current distribution on the BFO-CFO sample at nanoscale. It

Y.-H. Hsieh, Dr. C.-W. Liang, Prof. Y.-H. Chu
Department of Materials Science and Engineering
National Chiao Tung University
Hsinchu 30010, Taiwan
E-mail: yhc@nctu.edu.tw
J.-M. Liou, Prof. Y.-C. Chen
Department of Physics
National Cheng Kung University
Tainan 70101, Taiwan
B.-C. Huang, Prof. Y. P. Chiu
Department of Physics
National Sun Yat-Sen University
Kaohsiung 80424, Taiwan
Dr. Q. He
Advanced Light Source
Lawrence Berkeley National Laboratory
Berkeley, California 94720, USA
Prof. Q. Zhan
Department of Materials Physics and Chemistry
University of Science and Technology Beijing
Beijing 100083, China

DOI: 10.1002/adma.201201929

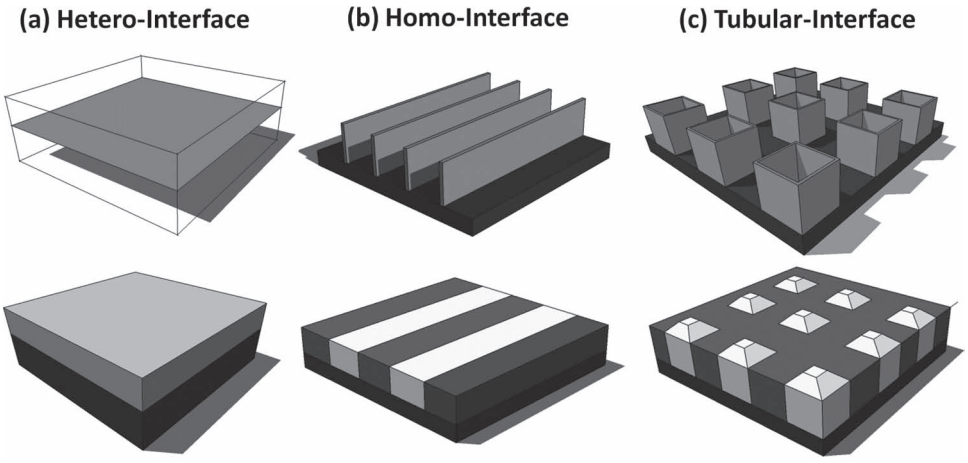

Figure 1. A huge playground of condensed matter physics: various types of complex oxide interfaces: (a) planar hetero-interface, (b) planar homo-interface, and (c) tubular hetero-interface.

clearly shows that the enhanced conduction was observed at the interface region between CFO pillar and BFO matrix, forming rectangular outlines in the current image under applied bias between ~0.05 to ~3 V. In Figure 2(c), the topography and current profiles indicate that the current maximum corresponds to the edge of the CFO pillar. This interface current conducts even under very small external sample bias of 0.05 V. Figure 2(d) displays local current versus voltage (*I*–*V*) curves measured by CAFM for the regions near interface and the matrix. Unlike in the matrix, which possesses undetectable currents under the range of testing bias, the turn-on voltages show the local conduction at the interface is much lower, and the currents decrease abruptly once the detecting AFM tip moves away from the interface. Moreover, when positive sample bias is applied, the *I*–*V* curves at the interfaces show the diode-like behavior, suggesting complex conduction behaviors in this system.

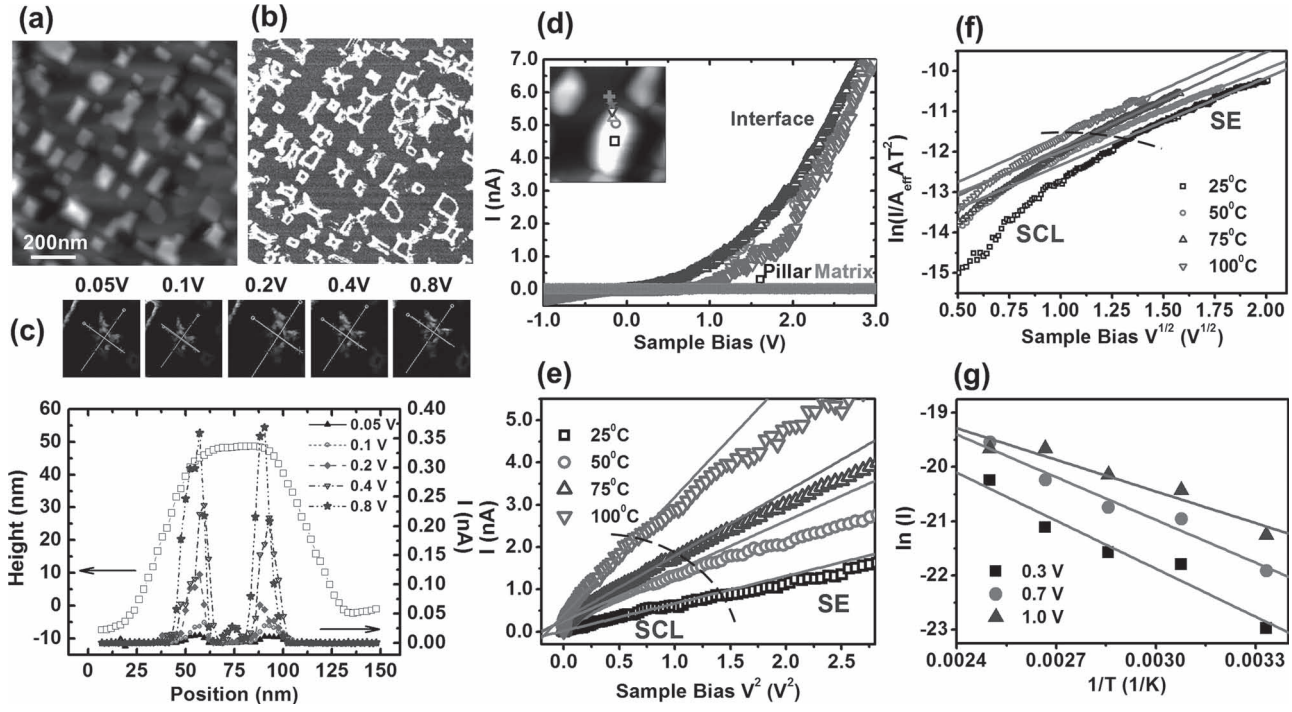

Figure 2. (a) Topography and (b) conducting AFM images taken at the same area with a sample bias of 0.05 V applied to the sample surface. (c) Comparison between topography and current profiles in the same cross-section. (d) *I-V* curves measured near and off the interface. The symbol dots on the inset AFM image indicated the positions to measure the *I-V* curves plotted in the same symbol. (e)(f) *I*–*V* curves measured at different temperature, which show the dependence of space charge limited (SCL) mechanism at low voltages and Schottky emission (SE) mechanism at high voltages, respectively. (g) Arrhenius plots of the SCL region, which shows the fitted activation energy is about 0.22 eV.

In order to investigate the transport mechanism at the interface, *I–V* curves at various temperatures were measured and fitted considering four typical models, i.e., Schottky emission, $\ln(I/T^2) \propto V^{1/2}/T$; Poole-Frenkel emission, $\ln(I/V^2) \propto V^{1/2}/T$; Fowler-Nordheim tunneling, $\ln(I/V^2) \propto -1/V$, and space charge limited mechanism, $I \propto V^2$.[21] After performing careful analysis on the experimental data and the fitting models, two mechanisms are determined to explain the transport behaviors at the interface. At low voltages (<1.5 V at room temperatures), the current shows linear dependence with the square of the bias voltage (Figure 2(e)), which implies the domination of space charge limited (SCL) mechanism, while at high voltages, *I–V* curves follow the dependence of Schottky emission (SE) mechanism (Figure 2(f)). The SE fitting in Figure 2(f) gives an optical dielectric permittivity of 3.0 ± 0.8, which is a reasonable value for oxides, and a Schottky barrier height of 0.41 ± 0.03 eV. The small Schottky barrier is why the small turn-on voltage works for conduction at the interface. On the other hand, SCL mechanism dominated at low voltages had also been found in previous studies of ferroelectric surfaces, where the polarization bound charges create a space-charge-like region and cause the dependence of $I \propto V^2$.[22,23] At the BFO-CFO interface, the charge (either polarity or ferroelectric) discontinuity might be the origin of the SCL like behaviors. Figure 2(e) and 2(f) show the conduction current increasing with the temperature. The activation energy extracted from the Arrhenius plots of the SCL region is about 0.2–0.3 eV, which indicates the energy barrier for creating free carriers.

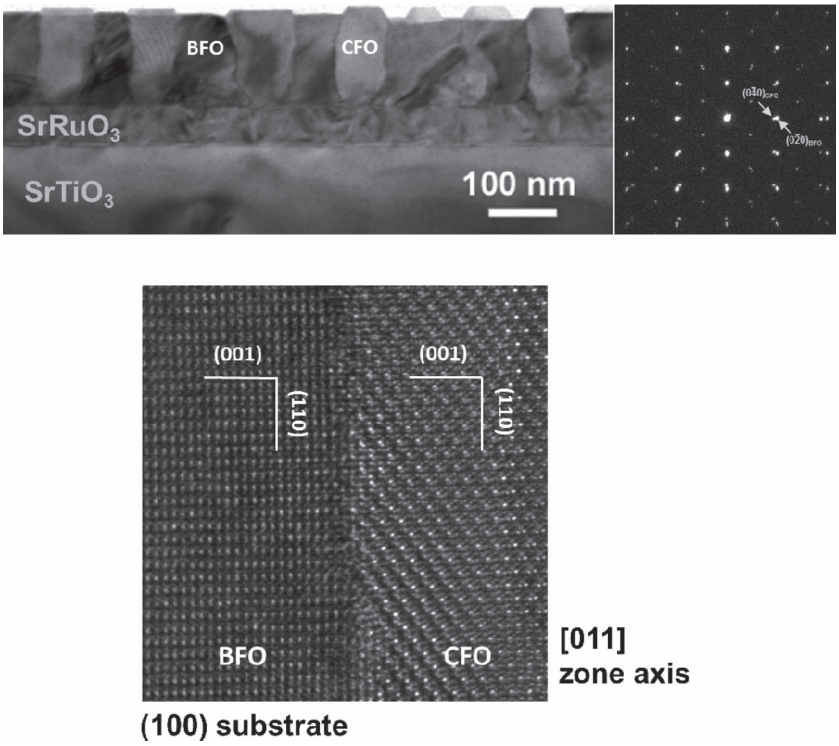

Figure 3. (a) the typical cross-sectional morphology of BFO-CFO thin film. (b) the typical electron diffraction patterns along the [100] axis. (c) a high-resolution image of the BFO-CFO interface with the incident beam along [110] direction.

Intriguing conducting behaviors are revealed at the interface, the next key investigation is to explore the possible origin of this local conduction. At first step, we have employed transmission electron microscopy (TEM) to explore structural insights close to oxide tubular interfaces. The typical cross-sectional morphology of BFO-CFO thin film is shown in **Figure 3**(a). It's clear that perovskite BFO and spinel CFO phases spontaneously separated after heteroepitaxial growth on a single-crystal (001) STO substrate. The CFO nanopillars alternate with ferroelectric BFO matrix and grow perpendicular to the substrate from bottom to top. It is worth to note that all of the CFO pillars form facets at the film surface, which is consistent with our AFM data (Figure 2(a)). Figures 3(b) is the typical electron diffraction pattern along the [100] zone axis. It suggests the two phases have a cube-on-cube orientation relationship: CFO [001] (110)//BFO [001] (110), which agrees with the XRD measurements. Figure 3(d) gives us a high-resolution image of the BFO-CFO interface with the incident beam along [110] direction. One should note that the sharp interface between CFO and BFO lies in the {110} orientation, similar to the BFO-$NiFe_2O_4$ system reported before.[24] In this kind of {110} interface, the octahedron in the perovskite contact directly to those in the spinel phase to lower the interface energy. The octahedron is much less perfect as inside the nearby crystals. In order to accommodate a high misfit strain, semicoherent interface was typically found in this kind of the interface. Parts of the octahedron are highly distorted or even disrupted. The modification of the chemical bonds at the interface would lead to changes in electronic structure, giving the population of additional states at the interface, which in turn can modify the electronic properties of the interface.

According to TEM study, structural discontinuity has been observed. The expected consequence of this structural change at the interface is the modification of electronic structure at the interface. Recently, the cross-sectional scanning tunneling microscopy and spectroscopy (XSTM/S) has been applied to explore the electronic structures across oxide interfaces with atomic resolution,[25] providing direct experimental insights into the origin of electrical conductivity. Therefore, to further look for the implication of the local conduction at this interface, the cross-sectional scanning has been applied to explore the electronic structure near the interface. The location of the interfaces between substrate, CFO, and BFO can be identified referring to the electronically specific tunneling spectra. **Figure 4**(a) shows a cross-sectional spectroscopic image of the epitaxial hetero-structure. The blue dotted line in Figure 4(a) indicates the position of the interface between the nanostructures and the substrate. Recording the interface makes it possible to investigate the electronic property of the vertical Interfaces. A band alignment across the BFO/CFO interface has be shown in Figure 4(b) in more detail using tunneling spectra

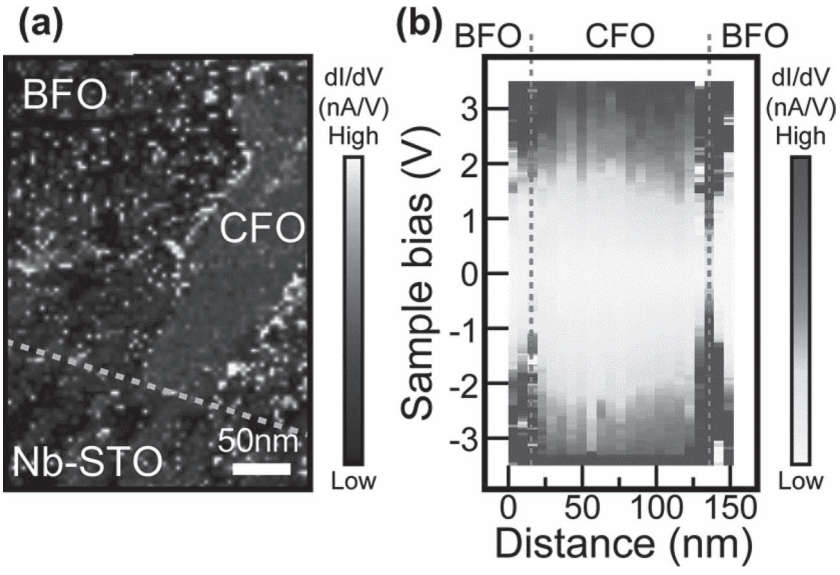

Figure 4. The cross-sectional scanning tunneling microscopy and spectroscopy near the interface. (a) a cross-sectional spectroscopic image of the epitaxial hetero-structure. The blue dotted line indicates the position of the interface between the nanostructures and the substrate. (b) a reconstructed band alignment to reveal the variation of the band-gap size across the BFO/CFO interface.

measurements. The resulting tunneling spectra in Figure 4(b) is plotted as the differential tunneling current *dI/dV* as a function of the sample bias across the interface of BFO/CFO. Spectral analyses of the sequentially layered electronic characteristics across the BFO/CFO interface illustrate the spatial variation of tunneling currents near Fermi level of the system. Briefly, the variation of the band-gap size across the BFO/CFO interface can be spatially analyzed from the region with zero tunneling current. The observation reveals that band-gap size shrinks across the interfaces of BFO/CFO. The decreased size in band gap shows additional interface states or electronic structure modifications due to atomic discontinuity, which can be an origin of the enhanced local conduction.

Based on the observation and analysis from TEM, CAFM, and XSTM measurements, we now turn to the possible conduction mechanism of this interface. To understand this local conduction, it is a critical step to know how the two phases bond at the interface. In a peroviste/spinel system, a seminal study[24] has pointed out that the most stable configuration is formed by a semi-coherent interface combined with $[BiFeO]^{4+}$ from BFO and $[[Co,Fe]O_2]^{-1.5}$ from CFO to minimize the interface charging and maintain the structural continuity across the interface (**Figure 5**(a)). Of particular interest is the nature of this semi-coherent interface. From the schematic of each {110} plane shown in Figure 5(a), the formation of the interface possesses at least 3 characteristics: 1) polarity discontinuity due to the unbalance charge, 2) ferroelectric ordering discontinuity attributed from ferroelectric BFO and non-ferroelectric CFO, and 3) the modification of the chemical bonds at the interface. These would lead to changes in electronic structure, giving the population of additional states at the interface. Two possible scenarios are constructed based on the energy barrier extracted from CAFM measurements (as summarized in Figure 5(b)). a) Single electron is trapped by oxygen vacancies in perovskites/spinels interfaces and this implies that the oxygen vacancy concentration play a key role to the conduction at BFO-CFO interface.[21] Interfaces, thereof, become the sink to attract oxygen vacancies. Each oxygen vacancy acts like a donor to provide electrons to the conduction. b) The segregation of Fe^{3+} ions close to the interface compensates the characteristics of the discontinuity and as a consequence, several orders change in resistivity is expected due to semiconducting behavior in Fe-rich CFO.[26] The activation energy in these scenarios is all very close to the energy acquired from CAFM measurements (0.25 eV). Further experiments need to be designed and performed to verify the dominated mechanism.

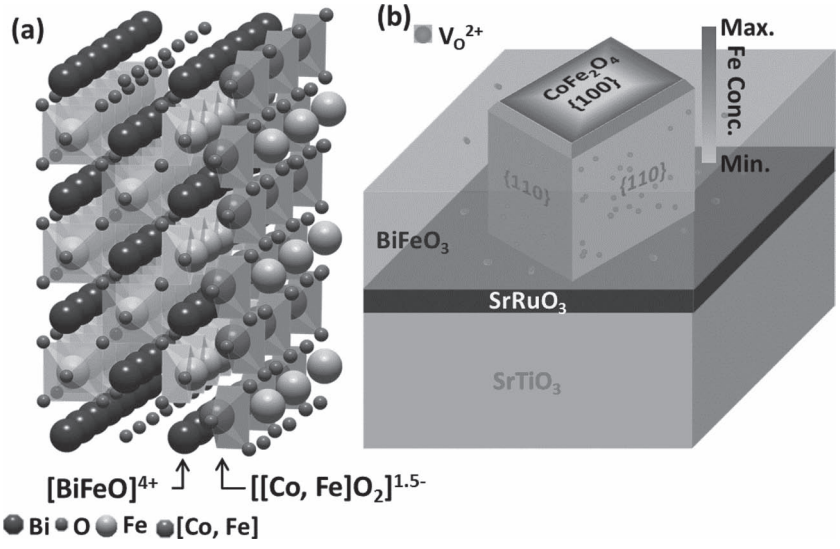

Figure 5. A summarized schematic for three possible driving force to the local conduction at BFO/CFO interface. (a) the boundary condition of BFO/CFO interface shows the polarity, ferroelectricity, and structure discontinuity (b) the outcome of those mentioned in (a) points out two possible explaination: one is large oxygen vacancy concentration close to the interface and the other the segregation of iron ions near the interfaces.

To sum up, self-assembled hetero-epitaxial nanostructures provide a huge playground to design new intriguing functionalities. The strong coupling between nanopillars and matrix mediated by the interface plays a crucial role to determine the properties of the system. However, in this study, we went back to re-examine the system by taking BFO-CFO as a model system and showed the local

conduction at the interface. The detailed measurements by CAFM and XSTM suggest the accumulation of oxygen vacancies or segregation of Fe^{3+} ions in CFO close to the interface to minimize the interfacial energies is the origin of this conduction. Thus, this study demonstrates that in such a nanostructure, the interface can not only be the medium to the coupling between phases, but also be a new state of the matter. The design concepts used in current hetero-interfaces and homo-interfaces, such as the interaction, frustration, discontinuity of lattice, charge, orbital, and spin degrees of freedom, should also be applicable to the new complex oxide tubular interface. Our study demonstrates a novel concept on oxide interface design and opens a pathway alternative for the explorations of diverse functionalities in complex oxide interfaces.

Experimental Section

During pulsed laser deposition, a composite target with 65% BFO and 35% CFO (molar ratio) was used, and samples were grown at 700 °C in O_2 (200 mTorr) and cooled with 500 Torr O_2 to minimize the creation of oxygen vacancies. Microstructural investigations have been carried out by using an FEI Tecnai F20 with the information limit of 1.4 Å. Conductive atomic force microscopy (CAFM) with temperature variable environment is performed by a commercial scanning probe microscope system (Veeco Escope AFM). Pt-coated tip with force constant about 2.8 N/m was used for measuring currents. For STM studies, the sample was cleaved in situ and measurements were performed from the cross-sectional geometry in an ultrahigh vacuum (UHV) chamber with a base pressure of ~5×10^{-11} Torr. In addition, scanning tunneling spectroscopy (STS) images were simultaneously acquired at ~100 K temperature.

Acknowledgements

The work at national Chiao Tung university is supported by the National Science Council, R.O.C., under contract No. NSC 100-2119-M-009-003. The work at national Cheng Kung university is supported by the National Science Council, R.O.C., under contract No. NSC 99-2112-M-006-012-MY3.

Received: May 13, 2012
Published online: July 13, 2012

[1] H. Y. Hwang, Y. Iwasa, M. Kawasaki, B. Keimer, N. Nagaosa, Y. Tokura, *Nat. Mater.* **2012**, *11*, 103.
[2] H. Takagi, H. Y. Hwang, *Science* **2010**, *327*, 1601.
[3] A. Ohtomo, H. Y. Hwang, *Nature* **2004**, *427*, 423.
[4] S. Thiel, G. Hammerl, A. Schmehl, C. W. Schneider, J. Mannhart, *Science* **2006**, *313*, 1492.
[5] J. Chakhalian, J. W. Freeland, G. Srajer, J. Strempfer, G. Khaliullin, J. C. Cezar, T. Charlton, R. Dalgliesh, C. Bernhard, G. Cristiani, H.-U. Habermeier, B. Keimer, *Nat. Phys.* **2006**, *2*, 244.
[6] P. Yu, J. S. Lee, S. Okamoto, M. D. Rossell, M. Huijben, C. H. Yang, Q. He, J. X. Zhang, S. Y. Yang, M. J. Lee, Q. M. Ramasse, R. Erni, Y. H. Chu, D. A. Arena, C. C. Kao, L. W. Martin, R. Ramesh, *Phys. Rev. Lett.* **2010**, *105*, 027201.
[7] T. Choi, Y. Horibe, H. T. Yi, Y. J. Choi, W. D. Wu, S. W. Cheong, *Nat. Mater.* **2010**, *9*, 253.
[8] H. Béa, M. Bibes, F. Ott, B. Dupe, X.-H. Zhu, S. Petit, S. Fusil, C. Deranlot, K. Bouzehouane, A. Barthélémy, *Phys. Rev. Lett.* **2008**, *100*, 017204.
[9] L. W. Martin, Y. H. Chu, M. B. Holcomb, M. Huijben, P. Yu, S. J. Han, D. Lee, S. X. Wang, R. Ramesh, *Nano Lett.* **2008**, *8*, 2050.
[10] J. Seidel, L. W. Martin, Q. He, Q. Zhan, Y. H. Chu, A. Rother, M. E. Hawkridge, P. Maksymovych, P. Yu, M. Gajek, N. Balke, S. V. Kalinin, S. Gemming, F. Wang, G. Catalan, J. F. Scott, N. A. Spaldin, J. Orenstein, R. Ramesh. *Nat. Mater.* **2009**, *8*, 229.
[11] J. Guyonnet, I. Gaponenko, S. Gariglio, P. Paruch, *Adv. Mater.* **2011**, *23*, 5377.
[12] J. L. MacManus-Driscoll, *Adv. Funct. Mater.* **2010**, *20*, 2035.
[13] H. Zheng, J. Wang, S. E. Lofland, Z. Ma, L. Mohaddes-Ardabili, T. Zhao, L. Salamanca-Riba, S. R. Shinde, S. B. Ogale, F. Bai, D. Viehland, Y. Jia, D. G. Schlom, M. Wuttig, A. Roytburd, R. Ramesh, *Science* **2004**, *303*, 661.
[14] S. A. Harrington, J. Zhai, S. Denev, V. Gopalan, H. Wang, Z. Bi, S. A. T. Redfern, S. H. Baek, C. W. Bark, C. B. Eom, Q. X. Jia, M. E. Vickers, J. L. MacManus-Driscoll, *Nat. Nanotechnol.* **2011**, *6*, 491.
[15] A. P. Chen, Z. X. Bi, C. F. Tsai, J. H. Lee, Q. Su, X. H. Zhang, Q. X. Jia, J. L. MacManus-Driscoll, H. Y. Wang, *Adv. Funct. Mater.* **2011**, *21*, 2423.
[16] J. Xiang, W. Lu, Y. Hu, Y. Wu, H. Yan, C. M. Lieber, *Nature* **2006**, *441*, 489.
[17] Z. Fan, H. Razavi, J. W. Do, A. Moriwaki, O. Ergen, Y. L. Chueh, P. W. Leu, J. C. Ho, T. Takahashi, L. A. Reichertz, S. Neale, K. Yu, M. Wu, J. W. Ager, A. Javey, *Nat. Mater.* **2009**, *8*, 648.
[18] S. C. Liao, P. Y. Tsai, H. J. Liu, J. C. Yang, S. J. Lin, C. H. Lai, Y. H. Chu, *ACS Nano* **2011**, *5*, 4118.
[19] H. Zheng, F. Straub, Q. Zhan, P. L. Yang, W. K. Hsieh, F. Zavaliche, Y. H. Chu, U. Dahmen, R. Ramesh, *Adv. Mater.* **2006**, *18*, 2747.
[20] R. K. Mishra, G. Thomas, *J. Appl. Phys.* **1977**, *48*, 4576.
[21] J. Seidel, P. Maksymovych, Y. Batra, A. Katan, S.-Y. Yang, Q. He, A. P. Baddorf, S. V. Kalinin, C.-H. Yang, J.-C. Yang, Y.-H. Chu, E. K. H. Salje, H. Wormeester, M. Salmeron, R. Ramesh, *Phys. Rev. Lett.* **2010**, *105*, 197603.
[22] P. W. M. Blom, R. M. Wolf, J. F. M. CillessenI, M. P. C. M. Krijn, *Phys. Rev. Lett.* **1994**, *73*, 2107.
[23] S. Farokhipoor, B. Noheda, *Phys. Rev. Lett.* **2011**, *107*, 127601.
[24] Q. Zhan, R. Yu, S. P. Crane, H. Zheng, C. Kisielowski, R. Ramesh, *Appl. Phys. Lett.* **2006**, *89*, 172902.
[25] Y. P. Chiu, Y. T. Chen, B. C. Huang, M. C. Shih, J. C. Yang, Q. He, C. W. Liang, J. Seidel, Y. C. Chen, R. Ramesh, Y. H. Chu, *Adv. Mater.* **2011**, *23*, 1530.
[26] G. H. Jonker, *J. Phys. Chem. Solids* **1959**, *9*, 165.